

## **Helmholtz cage design and validation for nanosatellites HWIL testing**

DA SILVA, Rodrigo Cardoso, ISHIOKA, Igor Seiiti Kinoshita, CAPPELLETTI, Chantal, BATTISTINI, Simone <<http://orcid.org/0000-0002-0491-0226>> and BORGES, Renato Alves

Available from Sheffield Hallam University Research Archive (SHURA) at:  
<http://shura.shu.ac.uk/24854/>

---

This document is the author deposited version. You are advised to consult the publisher's version if you wish to cite from it.

### **Published version**

DA SILVA, Rodrigo Cardoso, ISHIOKA, Igor Seiiti Kinoshita, CAPPELLETTI, Chantal, BATTISTINI, Simone and BORGES, Renato Alves (2019). Helmholtz cage design and validation for nanosatellites HWIL testing. IEEE Transactions on Aerospace and Electronic Systems, p. 1.

---

### **Copyright and re-use policy**

See <http://shura.shu.ac.uk/information.html>

# Helmholtz cage design and validation for nanosatellites HWIL testing

Rodrigo Cardoso da Silva, Igor Seiti Kinoshita Ishioka, Chantal Cappelletti, Simone Battistini, and Renato Alves Borges.

**Abstract**—This paper deals with the design, realization and testing of an Earth magnetic field simulator, that allows to validate hardware in the loop algorithms, as well as to test new actuators. The design is driven by typical small satellites functional requirements. The subsystems that compose the simulator are described in detail. The validation of the simulator is performed by assessing its functioning, the uniformity of the recreated magnetic field and the functionality of a magnetorquer.

**Index Terms**—Helmholtz cage, HWIL simulation, Attitude Determination and Control Systems, Small Satellites

## I. INTRODUCTION

A Helmholtz cage is a device that is capable of producing a controlled magnetic field. The use of such a system is related to several research activities in various fields [1], [2], [3], [4], [5]. Among several configurations of magnetic field simulators, the Helmholtz cage is considered one of the simplest [6]. It is composed, in fact, by two parallel coils only. If the structure is perfectly symmetric and the coils are sufficiently close one to each other, it is possible to generate a uniform magnetic field in one direction. In order to generate a magnetic field in the three dimensions of space, three orthogonal pairs of coils shall be used.

The magnetic field simulator described in this paper has been constructed inside the Laboratory of Simulation and Control of Aerospace Systems (LSCAS) of the University of Brasília (UnB), Brazil. The system described in this paper is paired to an air-bearing platform that is capable of simulating the attitude motion of a nanosatellite [7]. The aim of this system is to provide an Hardware-In-The-Loop (HWIL) facility for Attitude Determination and Control Systems (ADCS) of nanosatellites. Magnetic attitude control systems are very common in small satellites, due to their simplicity and low power consumption [8], [9]. In this context, an Earth Magnetic Field Simulator (EMFS) can be used for several applications, such as the testing of algorithms for attitude determination and control, HWIL testing of sensors and actuators [10], [11], [12] and satellites functional tests [13].

R. C. da Silva is with the Department of Electrical Engineering, University of Brasília, Brasília, Federal District, 70910-900 BR e-mail: rc-silva@lara.unb.br.

R. C. da Silva and R. A. Borges are with Department of Electrical Engineering, University of Brasília. I. S. K. Ishioka and S. Battistini are with Faculdade Gama, University of Brasília. C. Cappelletti is with the Department of Mechanical, Materials and Manufacturing Engineering, University of Nottingham.

Manuscript accepted January 27, 2019.

This paper describes in detail the design, realization and testing of a system made of commercial off the shelf components for HWIL magnetic field simulations. The realization of such a system and its use for ADCS applications go beyond the simple construction of a simulator of the Earth magnetic field. In the past, this has been treated in papers that focused mainly on constructive aspects such as the field intensity and uniformity generated with the Helmholtz cage or the closed loop control of the coils current [3], [5]. Apart from giving a detailed description of all these features for the proposed system, the original contributions of this paper lie in the set up of a fully integrated simulator for ADCS studies and in its validation in a HWIL environment, which aligns to the necessities of actual nanosatellites missions. The HWIL simulator is composed of the EMFS, an orbital propagator, a PID controller for coils current, computer vision software for pose estimation and magnetic actuators. The validation is performed through functional tests that validate both the designed EMFS and its use in an HWIL environment. A preliminary version of this work [14] demonstrated the capability of obtaining a uniformity region that allows the test of magnetic actuators for small satellites such as 3U CubeSats or even larger ones [15], [16]. The uniformity region of the proposed EMFS is larger than those achieved in [3] and [5].

This paper is organized as follows. Section II will present the requirements and the design of the EMFS. Section III will describe the realization of the EMFS and of the other hardware and software components that enter in the HWIL simulations. Section IV will show the tests that validate the design of the simulator. Conclusions will be given in Section V.

## II. DESIGN OF THE EMFS

### A. Requirements

The main requirement of the proposed simulator is the capability of generating the magnetic profiles of a typical nanosatellite orbit. Usually, nanosatellites are placed in LEO (Low Earth Orbit). As a matter of fact, the Earth Magnetic Field intensity decreases with the altitude, therefore, if the EMS is capable of recreating the field at very low altitudes, it will be also able to recreate higher orbits conditions. For this purpose, the altitude of 100 km is studied and the magnetic field intensity in this case is shown in Fig. 1, having in mind that the field distribution depicted in this figure represents only an approximation, since the Earth magnetic field is not constant and slowly changes.

As it can be seen in Fig. 1, the maximum magnetic field intensity obtained at this altitude is about  $60\mu T$ , which means

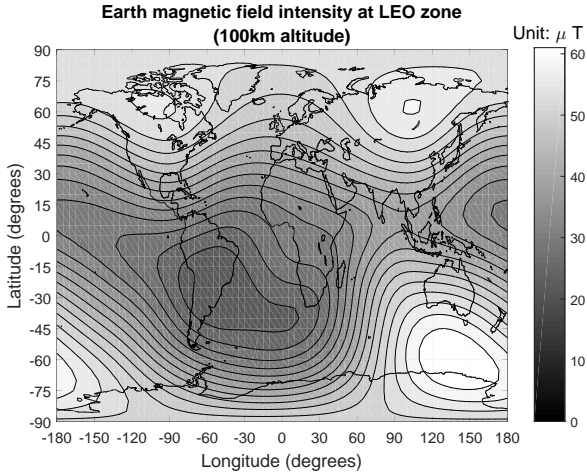


Fig. 1: Approximate current field intensity of the Earth magnetic field at 100 km.

that, in order to simulate any orbit, the simulator must be capable of providing at least this magnetic field intensity when combining the effects of all of its coils.

Another requirement concerns the magnetic field in the laboratory environment, which must be nullified when performing the experiments. In other words, the simulator must be capable of generating both the magnetic field of the laboratory and the magnetic field of the desired orbit.

Also, considering that the nanosatellite testbed is placed at the center of the Helmholtz cage, the magnetic field intensity measured by the testbed must be homogeneous and it must depend only on the current orbit position being simulated regardless of the orientation of the testbed. In other words, the magnetic field in the center of the cage must have considerable uniformity in a volume that covers the entire nanosatellite testbed.

Considering all these aspects, the requirements of the proposed system may be summarized as: the generated magnetic field intensity must present, at maximum, 5% error from the intensity foreseen in the desired orbit; the desired field direction must present, at maximum, 5 degrees error from the direction foreseen in the desired orbit; the generated field must present at least a 40 cm homogeneous zone with a 0.5% variation tolerance, which is compatible with the size of a 3U CubeSat; and the cage must have sufficient magnetic field generation capacity to both nullify the laboratory field and generate the desired field.

### B. Mathematical modeling

The Helmholtz cage, shown in Fig. 2, is composed of three pairs of square, mutually orthogonal coils and forming a three axis orthogonal system. Before describing its physical realization, the requirements of Sec. II-A shall be quantified and the corresponding mathematical equations deduced. In particular, some of the design parameters of the cage shall be presented, such as  $\gamma$ , a dimensionless number that indicates the optimal distance between coils after selecting the desired cage size. For this, the equation of the magnetic field generated by



Fig. 2: Helmholtz cage design.

the cage in its interior must be first determined. The proposed methodology is to simplify this demonstration by considering only one pair of square coils and then extending the results to the other pairs [3], [5], [6]. Fig. 3 shows the adopted nomenclature and the reference system for one of the coils, which is placed centered with the coil.

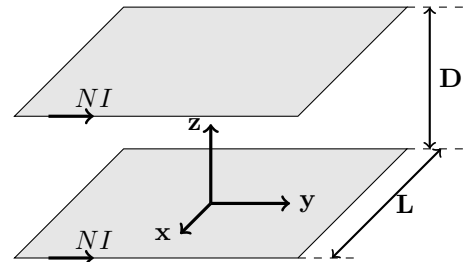


Fig. 3: Z-axis pair of coils.

To determine the magnetic field generated by a current flowing through a wire on a point P, one approach is to use the Biot-Savart law, which says that the infinitesimal magnetic field  $d\mathbf{B}$  generated by a current  $I$  passing through an infinitesimal length wire  $d\mathbf{l}$  is given by

$$d\mathbf{B} = \frac{\mu}{4\pi} \frac{I d\mathbf{l} \times \hat{\mathbf{r}}}{r^2} = \frac{\mu}{4\pi} \frac{I dl \sin\theta}{r^2} \hat{\mathbf{u}}, \quad (1)$$

where  $\mu$  is the magnetic permeability of the medium,  $r$  is the distance between the point where the magnetic field is evaluated and the infinitesimal wire position,  $\hat{\mathbf{r}}$  is the unit vector of the distance between  $d\mathbf{l}$  and the point P, pointing to the point P,  $\hat{\mathbf{u}}$  is the unit vector orthogonal to both  $d\mathbf{l}$  and  $\hat{\mathbf{r}}$  vectors and pointing to the direction of the infinitesimal magnetic field  $d\mathbf{B}$ , and  $\theta$  is the angle between  $d\mathbf{l}$  and  $\hat{\mathbf{r}}$ .

Before applying the Biot-Savart law, it must be noticed that the problem may be further simplified by focusing on only one coil of a pair, since both coils generate the same magnetic field

pattern. Furthermore, the demonstration of the magnetic field of one coil may be divided in four parts, one for each side of the coil. Fig. 4 depicts the side of the coil to be analysed.

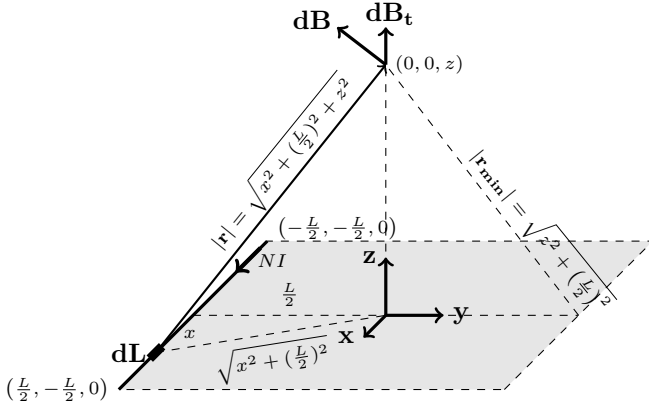


Fig. 4: Biot-Savart law applied to one side of a coil.

Applying the Biot-Savart law to one side,  $d\mathbf{B}$  is given by

$$d\mathbf{B} = \frac{\mu(NI)}{4\pi} \frac{dx}{r^2} \frac{\sin \theta}{r} \hat{\mathbf{u}}, \quad (2)$$

where  $N$ , the number of coil turns of one of the six coils of the cage, is introduced to compute the infinitesimal field generated by each turn. To determine  $\sin \theta$ , the distance  $r_{\min}$  is defined, which is the minimum distance between the coil side and the point where  $d\mathbf{B}$  is calculated, as can be seen in Fig. 5.

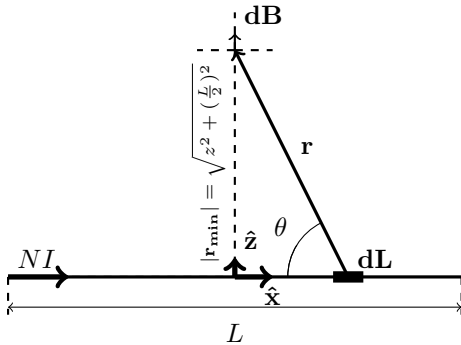


Fig. 5: View of plane formed by  $d\mathbf{l} \times \mathbf{r}$ , showing the angle  $\theta$  between  $d\mathbf{l}$  and  $\mathbf{r}$ .

From Eq. (2), using the fact that  $\sin \theta = \frac{r_{\min}}{r}$  (see Fig. 5), it follows

$$d\mathbf{B} = \frac{\mu(NI)}{4\pi} \frac{r_{\min}}{r^2} dx \hat{\mathbf{u}}, \quad (3)$$

To determine the magnetic field along the  $z$  axis, only the  $d\mathbf{B}_t$  component must be determined, which is the component tangential to the  $z$  axis, as shown in Fig. 4. It is not relevant to determine the  $z$ -axis normal component  $d\mathbf{B}_n$ , since this component is nullified when summing the contributions of the entire coil due to its symmetry. As can be seen in Fig. 6,  $d\mathbf{B}_t = \cos \alpha d\mathbf{B} \hat{\mathbf{z}} = \frac{L/2}{r_{\min}} d\mathbf{B} \hat{\mathbf{z}}$ .

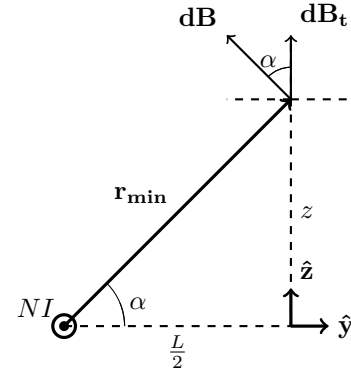


Fig. 6: View of the  $zy$  plane, showing the angle  $\alpha$  between  $d\mathbf{B}$  and its  $z$ -axis component  $d\mathbf{B}_t$ .

Substituting the expression for  $d\mathbf{B}$  in  $d\mathbf{B}_t$  and integrating  $d\mathbf{B}_t$  along  $L$  gives

$$\begin{aligned} \mathbf{B}_{side}(z) &= \int d\mathbf{B}_t = \int \frac{L/2}{r_{\min}} d\mathbf{B} \hat{\mathbf{z}} = \\ &= \int \frac{L/2}{r_{\min}} \frac{\mu(NI)}{4\pi} \frac{r_{\min}}{r^2} dx \hat{\mathbf{z}} = \\ &= \int_{-L/2}^{L/2} \frac{\mu(NI)}{4\pi} \frac{L/2 dx}{r^3} \hat{\mathbf{z}} \\ &= \frac{\mu(NI)}{4\pi} \int_{-L/2}^{L/2} \frac{L/2 dx}{(z^2 + (L/2)^2 + x^2)^{3/2}}, \end{aligned}$$

in which the magnetic field is parameterized by the distance  $z$  along the axis of the coil. Observing that  $z$  is a constant parameter within this integral and using the identity  $\int \frac{dx}{(a^2 + x^2)^{3/2}} = \frac{x}{a^2 \sqrt{a^2 + x^2}}$ , the magnetic field generated by one side of the coil is obtained as

$$B_{side}(z) = \frac{\mu NI}{\pi} \frac{L^2}{(4z^2 + L^2) \sqrt{4z^2 + 2L^2}}, \quad (4)$$

Multiplying the magnetic field in Eq. (4) by four to obtain the magnetic field generated by the four sides of a single coil and summing the magnetic field generated by both coils, the resulting magnetic field along the pair of coils axis is obtained as

$$B(z) = 4B_{side}(z) + 4B_{side}(z - D) \quad (5)$$

in which attention must be given to the points where the magnetic field is evaluated:  $z$  for the first coil and  $-(D - z)$  for the second coil. Developing Eq. (5), the total magnetic field of the pair of coils along its radial axis  $z$  is given by

$$B(z) = \frac{4\mu NI}{\pi L} \left( \frac{1}{\left[ \left( \frac{z}{L/2} \right)^2 + 1 \right] \sqrt{\left( \frac{z}{L/2} \right)^2 + 2}} + \dots \right. \\ \left. \dots + \frac{1}{\left[ \left( \frac{z-D}{L/2} \right)^2 + 1 \right] \sqrt{\left( \frac{z-D}{L/2} \right)^2 + 2}} \right) \quad (6)$$

Taking as a special case the center of the pair of coils, in which  $z = \frac{D}{2}$ , the total magnetic field in the center of the cage is obtained as

$$B_O \left( z = \frac{D}{2} \right) = \frac{8\mu_0 NI}{\pi L} \frac{1}{\left( \left( \frac{D}{L} \right)^2 + 1 \right) \sqrt{\left( \frac{D}{L} \right)^2 + 2}} \quad (7)$$

Again from Eq. (6), the total magnetic field along the coil axis may be seen as

$$B(z) = \frac{4\mu_0 NI}{\pi L} \left[ f \left( \frac{z}{L/2} \right) + f \left( \frac{z-D}{L/2} \right) \right] \quad (8)$$

in which the auxiliar function  $f$  is defined as:

$$f(\alpha) = \frac{1}{(\alpha^2 + 1)\sqrt{\alpha^2 + 2}}, \quad \alpha = \frac{z}{L/2}. \quad (9)$$

The  $\alpha(z)$  parameter is a function of the point  $z$  where the field uniformity will be studied. Considering that it is desired to study the field uniformity of the cage at its center, the  $\alpha$  parameter is set as  $\alpha = \frac{D/2}{L/2} = \frac{D}{L} = \gamma$ . From this, it can be seen that  $\gamma$  - the construction parameter of the cage - is defined as the ratio between the distance from a coil to the cage center ( $D/2$ ) and half the length of the side of a coil ( $L/2$ ).

Having this expression for the magnetic field, the optimal construction parameter  $\gamma_{optimal}$  may be determined. As one requisite for the cage is to maximize the field uniformity in its interior, the function to be minimized is  $\frac{dB}{d\gamma}$ , *i.e.* the variation of the field with relation to the construction parameter  $\gamma$ . For this, the  $\gamma$  value where this variation is minimized must be determined. This may be accomplished by first calculating the value of  $\gamma$  corresponding to  $\frac{d^2 B}{d\gamma^2} = 0$ .

From Eq. (8) with  $z = D/2$  and considering  $\alpha|_{z=D/2} = \gamma$ , the first and second derivatives are given by

$$\frac{dB(\gamma)}{d\gamma} = \frac{4\mu_0 NI}{\pi L} [f'(\gamma) - f'(-\gamma)] \quad \text{and} \quad (10)$$

$$\frac{d^2 B(\gamma)}{d\gamma^2} = \frac{4\mu_0 NI}{\pi L} [f''(\gamma) + f''(-\gamma)]. \quad (11)$$

Considering that the first derivative of  $f(\gamma)$  is given by

$$\frac{df(\gamma)}{d\gamma} = -\frac{\gamma(5 + 3\gamma^2)}{(1 + \gamma^2)^2(2 + \gamma^2)^{3/2}} \quad (12)$$

it can be seen that  $\frac{dB(\gamma)}{d\gamma} = \frac{8\mu_0 NI}{\pi L} f'(\gamma)$ , since  $f'(-\gamma) = -f'(\gamma)$ . From this, Eq. (11) may be simplified as

$$\frac{d^2 B(\gamma)}{d\gamma^2} = \frac{8\mu_0 NI}{\pi L} \cdot f''(\gamma). \quad (13)$$

As the only varying part of  $\frac{d^2 B(\gamma)}{d\gamma^2}$  is the  $f''(\gamma)$  derivative, it is only required to obtain the roots of the  $f''(\gamma)$ . This leads to

$$\frac{d^2 f(\gamma_i)}{d\gamma_i^2} = \frac{2(6\gamma_i^6 + 18\gamma_i^4 + 11\gamma_i^2 - 5)}{(\gamma_i^2 + 1)^3(\gamma_i^2 + 2)^{5/2}} = 0, \quad i \in \{1, \dots, 6\}, \quad (14)$$

whose roots are  $\gamma_{1,2} = \pm 0.544505$  and  $\gamma_{3,4,5,6} = \pm 0.1189 \pm 1.2893 i$ . Since the optimal value for  $\gamma$  must be a positive real number, there is only one possibility, which is  $\gamma_1 = 0.544505$ . In fact, numerical simulations of the  $f'(\gamma)$  function in Eq. (12)

shows that the positive value  $\gamma_1 = 0.544505$  corresponds to a global minimum, whereas the negative value  $\gamma_2 = -0.544505$  corresponds to a global maximum, *i.e.* both points correspond to points in which the variation of the  $f'(\gamma)$  function is minimal. However, it must be noticed that the negative root  $\gamma_2 = -0.544505$  of the  $f'(\gamma)$  function simply represents the same optimal situation - minimal variation of  $f'(\gamma)$  - in the negative portion of the adopted reference, as if the second square coil was placed behind the first. Having the  $\gamma$  parameter determined, the optimal distance between the coils in a pair may be obtained as

$$D_{optimal} = \gamma_{optimal} L = 0.5445L. \quad (15)$$

### C. Theoretical field uniformity

As  $\gamma$  indicates the optimal relationship between  $D$ , the distance between two coils in a pair, and  $L$ , the length of the coils side, then the uniformity of the proposed cage may be studied for different tolerances in the value of the optimal  $\gamma$ . In Fig. 7 two effects are analysed: increases in the values for  $\gamma$  ( $\pm 2\%$  or  $\pm 5\%$  around its optimal value) and increases in the allowed variation interval of the ratio between  $B(z)$ , the magnetic field along one axis, and  $B(0)$ , the magnetic field at the center of the cage, namely the uniformity ratio (limits  $\pm 0.05\%$  and  $\pm 5\%$  in Fig. 7).

As it can be seen in Fig. 7, for a  $\pm 2\%$  variation in the value of  $\gamma$ , when considering a  $\pm 0.05\%$  tolerance in the uniformity ratio, the uniform magnetic field zone ranges from about  $0.28 \text{ m}$  (since the dotted curve leaves the  $\pm 0.05\%$  tolerance zone approximately between the positions  $-0.14 \text{ m}$  and  $0.14 \text{ m}$ , symmetrically) to  $0.56 \text{ m}$  (as the same occurs with the dot-and-dash curve between the positions  $-0.28 \text{ m}$  and  $0.28 \text{ m}$ ). It means that, even in this very strict scenario, the cage still can provide, in the worst case, a  $0.3 \text{ m} \times 0.3 \text{ m} \times 0.3 \text{ m}$  volume of uniform magnetic field, approximately. This is sufficient for conducting tests with 3U CubeSats, which is nowadays a very popular format for small satellites. Also, when considering a  $5\%$  variation in  $\gamma$  and the uniformity ratio, this volume increases to more than  $1 \text{ m}^3$ .

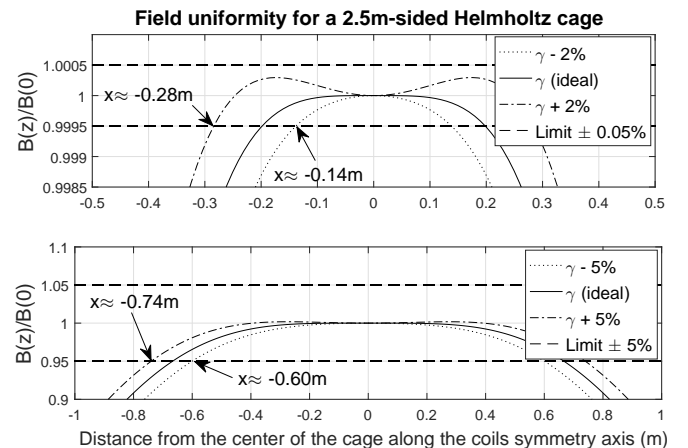


Fig. 7: Uniformity of the magnetic field generated along the symmetry axis of one pair of coils.

For illustration purpose, the maximum positioning error allowed when constructing the cage is calculated as follows. Considering a 2.5 m sided coil, the ideal distance between the coils in a pair must be

$$D_{optimal} = 0.5445 \cdot 2.5 \text{ m} = 1.36125 \text{ m} , \quad (16)$$

whereas, considering a 2% error in  $\gamma$ , this distance becomes

$$D = 0.5445(1 + 0.02) \cdot 2.5 \text{ m} = 1.388475 \text{ m} , \quad (17)$$

*i.e.*, the maximum allowed error when positioning the coils during the construction of the 2.5 m-sided cage must be 2.6 cm approximately, given the studied  $\pm 0.05\%$  tolerance. Also, as indicated by Fig. 7, this error is better to occur in the sense of increasing the distance between the coils in the proposed tolerance.

Therefore, it is important to guarantee minimum variation of the  $\gamma$  parameter during the construction of the cage by ensuring that the positioning error of the coils in a pair stay below the maximum allowed error for the desired tolerance. This caution is mandatory to provide the necessary precision for orbit simulations. In this work, the 0.05% variation limit for  $\gamma$  is sufficient for experiments with nanosatellites.

#### D. Principles of magnetorquer functioning

Magnetorquers are magnetic actuation devices used for satellite attitude control. The working principle of such devices is based on the generation of a torque by interaction with the geomagnetic field. The magnetorquers used in this work are basically solenoids, with and without magnetic cores.

Fig. 8 shows the set of 2 board units of the 3-axis actuators used in the testbed grouped in a stack of boards with the PC104 form factor. Each actuator is formed by three magnetorquers, two being cylindrical coils (X and Y axis) composed of EFI Aloy 79 magnetic core with the same design used in a previous version of the actuator [12]. The third magnetorquer is a cylindrical air coil (Z axis). Both the torquerods and the cylindrical coil were designed to operate nominally through a 5VDC power supply.

In order to briefly describe the functioning of magnetorquers, it suffices to analyze the torque generated by a magnetic dipole in a magnetic field. The magnetic torque  $\tau_m$  is given by Eq. (18),

$$\tau_m = \mathbf{m} \times \mathbf{B} , \quad (18)$$

in which  $\mathbf{m}$  is the magnetic moment and  $\mathbf{B}$  is the magnetic field. For control purposes, it is interesting to determine the dipole momentum  $\mathbf{m}$  necessary to generate the desired magnetic torque  $\tau$  [13]. Isolating  $\mathbf{m}$  in Eq. (18) leads to Eq. (19),

$$\mathbf{m} = \underbrace{\frac{\mathbf{B} \times \tau_m}{\|\mathbf{B}\|^2}}_{\mathbf{m}_n} + \underbrace{\lambda \mathbf{B}}_{\mathbf{m}_\theta} , \quad (19)$$

in which  $\mathbf{m}_n$  and  $\mathbf{m}_\theta$  are the normal and tangential components of  $\mathbf{m}$  relative to  $\mathbf{B}$  and  $\lambda$  is a scalar given by  $\lambda = \frac{\|\mathbf{m}\|}{\|\mathbf{B}\|} \cdot \cos \phi$ , being  $\phi$  the angle between  $\mathbf{m}$  and  $\mathbf{B}$ . Fig. 9 illustrates these vectors.

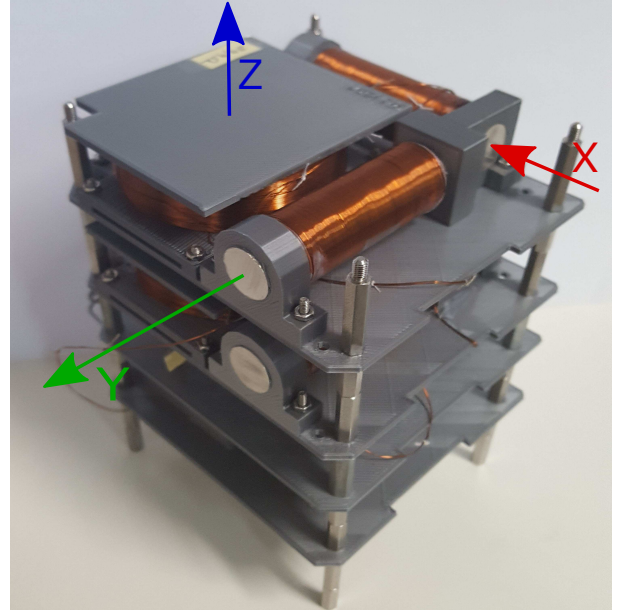


Fig. 8: A PC-104 standard stack with two magnetorquer modules developed at the LSCAS (UnB, Brazil).

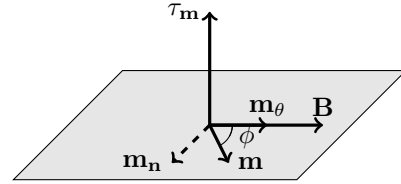


Fig. 9: Relationship between the  $\mathbf{B}$ ,  $\mathbf{m}$  and  $\tau$  vectors.

The necessary dipole momentum in the control maneuver can be generated by adjusting the current in the winding of each magnetorquer, accordingly to Eq. (21)

$$\mathbf{m} = [\mathbf{m}_x \ \mathbf{m}_y \ \mathbf{m}_z]^T , \quad (20)$$

$$\mathbf{m}_i = N_m \cdot I \cdot A \cdot \hat{\mathbf{i}} , \quad i \in \{x, y, z\} , \quad (21)$$

in which  $\hat{\mathbf{i}}$  is a unit vector pointing towards the selected magnetorquer axis,  $I$  is the current of the winding,  $N_m$  is the number of coil turns of the magnetorquer and  $A$  is the cross section area of the winding. When the magnetorquer is constituted by a magnetic core, its core magnetization must be taken into consideration for the computation of its dipole momentum. Due to the orthogonal configuration of the magnetorquers, any three-dimensional dipole momentum may be generated. It implies that any torque may be generated except torques along the direction of the environmental magnetic field  $\mathbf{B}$ , as a consequence of Eq. (18).

### III. REALIZATION OF THE EMFS

This section describes the implementation of the Earth Magnetic Field Simulator, including its mechanical and electrical characteristics, as well as a description of the developed software.



### A. Mechanical design

The mechanical description of the system comprises two main parts: the Helmholtz cage structure and the magnetorquers dimensioning.

a) *Helmholtz Cage*: The Helmholtz cage structure is made of aluminum U-profile metal bars, which is a paramagnetic material, *i.e.* a material with low magnetic permeability. The U-profile is squared, with 1 inch base and 1 inch side and  $3/32$  inch of thickness, and provides a gap in which the magnet wire loops are placed. Each aluminum bar is attached to the other through triangular supports with M5 stainless steel screws. Each of the six square structures is covered with magnet wires to form the Helmholtz cage windings and each coil is connected to its pair ensuring both magnetic fields of a pair add in the same direction.

Fig. 10 shows that the coils are arranged in a nested structure, which means that there is an inner, a middle and an outer pair. For this reason, the  $L/2$  parameter of the cage is not the same for all pairs and the cage is not a perfect  $2.5m$ -sided cube.  $L/2$  measures are  $1.25 m$ ,  $1.197 m$  and  $1.2235 m$  in the outer, middle and inner pairs of coils, respectively.

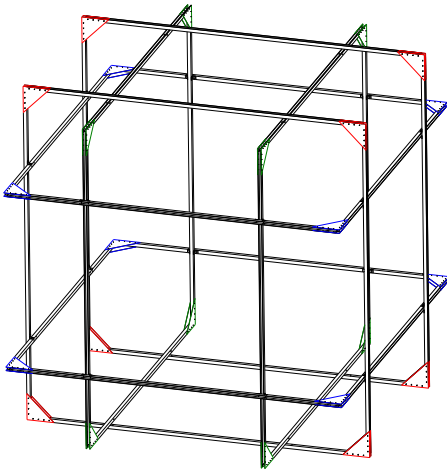


Fig. 10: Computer-Aided Design (CAD) of the Helmholtz cage.

b) *Magnetorquer*: In order to develop the torquerods - X and Y axis coils of the 3-axes actuator - a specific winder was developed [12]. This design is an optimized version of previous models, which updates the characteristics of the coil supports and the PC104 form factor board, but maintains the torquerods dimensions. Table I refers to the geometrical parameters of the torquerod magnetorquers shown in Fig. 11.

For the manufacturing of the air coil (Z axis) the enamelled copper wire was applied directly to its permanent structural support, that has a  $25.694 mm$  inner radius. In this version of the actuator, the structural supports and the board were 3D printed in PLA, which allowed fast prototyping.

### B. Electrical design

The electrical design of the EMF Simulator is composed mainly by three parts: the Helmholtz cage, the DC sources and the 3-axis magnetometer placed in the center of the cage.

Parameter	Description	Size (mm)
$L_c$	Core length	64.5
$L_b$	Winding length	48.5
$L_s$	Support thickness	8
$D_c$	Core diameter	12.7
$h_1$	Maximum winding height	23.91
$h_2$	Distance between winding and PCB	0.25
$h_3$	Clamp thickness	3.875
$h_4$	Support height	22.305
$t$	Thickness of the winding layers	5.48

TABLE I: Parameters of the X and Y axes magnetorquers.

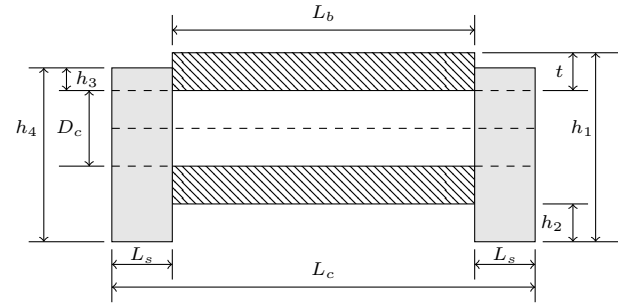


Fig. 11: Magnetorquer geometry.

The above mentioned hardware is connected to an external computer that performs the orbital simulations, calculates the attitude transformations and sends commands to the DC sources. In this way it is possible to run HWIL ADCS simulations.

The Helmholtz cage windings are made of AWG14 copper wires, whose nominal current is  $5.9A$  - which, in this work, is rounded to  $6A$  -, diameter is  $1.628 mm$  and resistance is  $8.282 \Omega/km$ . Each pair of coils has  $2N = 80$  turns of copper wire equally divided in each coil and a measured resistance of  $6.90 \Omega$ ,  $6.84 \Omega$  and  $6.57 \Omega$  in the outer, middle and inner pairs, respectively. This is coherent with the resistance-per-km parameter of the AWG14 copper wire, since each square coil has approximately  $400 m$  of wire, rounding up to about  $800 m$  for each pair of coils. Each pair of coils is connected to one Agilent 6032A DC sources, capable of providing up to  $60 V$  or  $50 A$ , in a  $1000 W$  maximum power consumption. These sources are connected to the external computer and remotely controlled through GPIB interface. To feedback the control loops of the cage, a HMR2300 magnetometer, manufactured by Honeywell, is placed in the exact center of the cage, fixed in the air bearing table base.

### C. Software design

The software of the EMF simulator is implemented in the external computer and is summarized by the steps shown in the flowchart of Fig. 12.

Initially, the software establishes the serial connection between the computer and the Sources A, B and C, which are used to control the current through the windings of the cage. Also, the current limits are set up in this step, preventing the simulation from generating currents above the nominal current of the windings of the cage. Using TLE (Two Line Element set) and SGP4, a simplified perturbation model, the

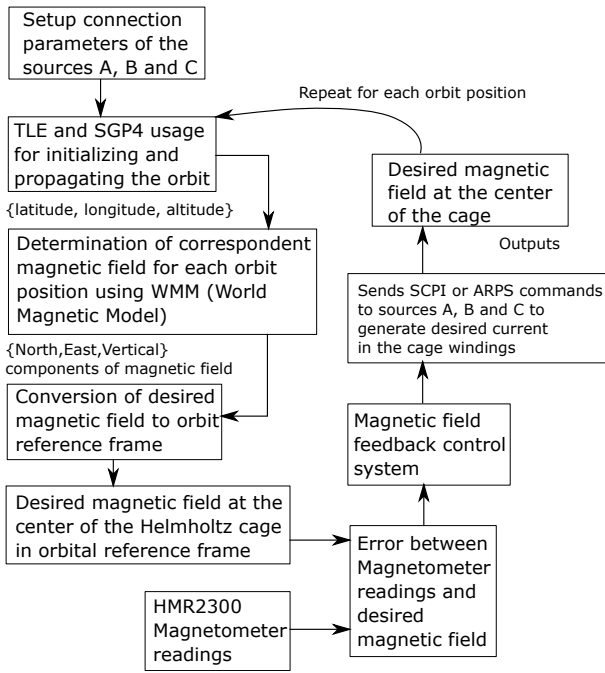


Fig. 12: HWIL EMF simulator flowchart

orbit is calculated along a certain time interval [17]. The intensity of the magnetic field is calculated based on the World Magnetic Model (WMM) published by the National Centers for Environmental Information of the National Oceanic and Atmospheric Administration (NOAA), which is updated every 5 years and used to obtain the North, East and Up components of the magnetic field corresponding to the set of all latitudes, longitudes and altitudes of the orbit points. It is interesting to notice that the International Geomagnetic Reference Field (IGRF) model could also be used to determine the magnetic field in a specific orbit, since both WMM and IGRF provide similar results. A relevant difference in these models is the nature of the data provided by each model: the data in the WMM model is only predicted, whereas in the IGRF model the data of the model is updated retrospectively. Considering that the cage axis are coincident with the orbital reference frame, the magnetic field vector must be transformed from the North-East-Up reference to the orbital reference frame. Finally, using the measurements of the HMR2300 magnetometer placed in the center of the cage and aligned with the cage axis, the magnetic field reference error is determined and used in a digital feedback PID-controlled system implemented in the software, in order to generate the desired magnetic field. These steps are repeated for each point of the entire simulated orbit.

Furthermore, a Computer Vision assisted Attitude Determination Software (CVADS) was developed in order to determine the attitude of the testbed. This software processes the image acquired from a webcam and, with aid of the ARUCO patterns - fiducial markers present in a library for Augmented Reality applications based on OpenCV - strategically placed upon the testbed, determines the orientation of the system [18]. This application runs as a server in the laboratory network and the measurements can be acquired from any computer in

this network through TCP/IP protocol. Fig. 13 illustrates the CVADS.

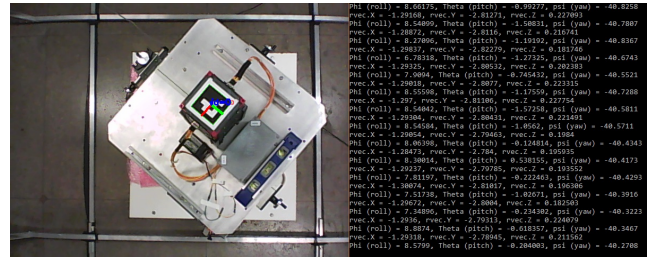


Fig. 13: CVADS application.

#### IV. VALIDATION OF THE SIMULATOR

In this section some experiments are proposed in order to evaluate the magnetic field simulation and the magnetorquer functioning performances. They are:

- Calibration of the magnetometer: the HMR2300 must be calibrated in order to carry out the magnetic experiments that follow. Even magnetic sensors with a reasonable quality such as the HMR2300 must be calibrated, since there are various sources of error that may affect it, such as misalignment errors, scale factor errors, null shift errors and hard and soft iron effect errors. Fig. 14 shows a set of measurements acquired from the sensor in as many orientations as possible before calibration. This figure shows that the ellipsoid is centered distant from the origin, which means that a high offset value is present, whereas the ellipsoid shape indicates different scaling factors in each axis. It can be noticed that the local magnetic field magnitude is around  $28\mu T$ , while the magnitude of the offset vector in this figure is  $90\mu T$ .

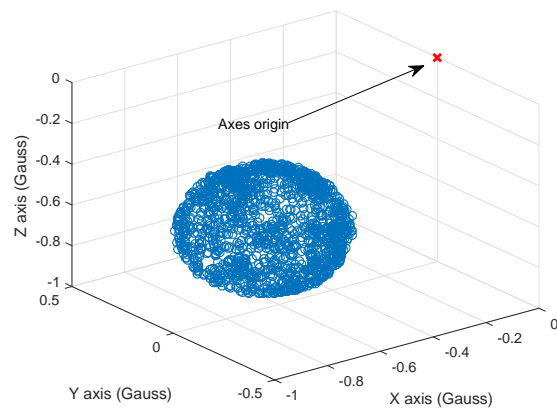


Fig. 14: Ellipsoid before calibration.

To mitigate the hard and soft iron effects as well as to compensate the measurements for the offset and scaling factors in each axis, the method described in [19] is used, assuming that the nonorthogonality of the sensor axes is negligible. The method in [19] consists in determining three scale factors ( $S_x, S_y, S_z$ ) and three field offset



values ( $O_x, O_y, O_z$ ) in order to transform the ellipsoid in Fig. 14 in an unit sphere centered at the origin. This procedure ensures that the measured field direction is correct. Then, to ensure that the measured field intensity is also correct, this unit sphere must be scaled with the local magnetic field intensity ( $B_{lab}$ ), which is obtained by checking the intensity indicated by the World Magnetic Model (WMM) with the coordinates of the LSCAS and comparing this intensity with that measured by other HMR2300 sensors available. Eq. (22) summarizes the adopted calibration procedure

$$\hat{\mathbf{B}} = B_{lab} \cdot \begin{bmatrix} \frac{1}{S_x} & 0 & 0 \\ 0 & \frac{1}{S_y} & 0 \\ 0 & 0 & \frac{1}{S_z} \end{bmatrix} \cdot \left( \mathbf{B} - \begin{bmatrix} O_x \\ O_y \\ O_z \end{bmatrix} \right), \quad (22)$$

in which  $\mathbf{B}$  is the uncorrected magnetic field measurement and  $\hat{\mathbf{B}}$  is the corrected measurement.

- Experiment 1: the goal of this experiment is to validate the capacity of the EMFS to generate the magnetic field of a typical nanosatellite orbit. The values of magnetic field obtained from the HMR2300 sensor are analyzed. Furthermore, a sampling time analysis of the system is provided, as well as the time constant of each pair of axis, considering the RL network model.
- Experiment 2: the uniformity of the generated magnetic field is evaluated and compared with the theoretical uniformity foreseen in Sec. II-C.
- Experiment 3: the simulator is validated by means of magnetic actuators. The magnetic field vector inside the Helmholtz cage is controlled to change its direction only in the xy plane with a 90 degrees amplitude. The magnitude of this vector is set to approximately 80% of the cage capacity. The y-axis magnetic actuators are turned on at their nominal capacity and the yaw angle of the testbed is measured with the CVADS.

#### A. Experiment 1: functionality test of the EMFS

The first consideration regards the sampling time of the software. During tests with various sampling times, which are set up with time delays introduced in the source code, the minimum sampling time ( $T_s$ ) was determined to be 3 s. This is strictly related with the time required by the software to send the voltage/current generation commands to the sources, which is approximately 1 s for each source. This sampling time is adequate for orbit simulations, since completing an orbital period typically lasts an hour, at least, and the magnetic field varies slowly.

A discrete PID controller is proposed to ensure that the magnetic field generated by the cage coincides with that required in the simulation. In this case, the control loop is summarized as a unit negative feedback loop with the PID controller and the Helmholtz cage model in the open loop

given by Eqs. 23 and 24, respectively,

$$I_k = I_{k-1} + K_p \cdot (e_k - e_{k-1}) + \frac{K_p T_s}{T_i} e_k + \frac{K_p T_d}{T_s} (e_k - 2e_{k-1} + e_{k-2}) \quad (23)$$

$$e_k = B_{reference-k} - B_{measured-k} \\ B_k = \kappa \cdot I_k, \quad (24)$$

in which  $\kappa$  is defined as the constant part of the term in Eq. (7),  $K_p$ ,  $T_s$  and  $T_i$  are the PID tunable constants, the discrete PID controller output  $I_k$  is determined using backwards Euler derivatives and the cage model is considered static. The consideration about the cage model being static is reasonable, since the RL network of each pair of coils has a time constant considerably smaller than the simulation sampling time (3 s). Considering the resistance values of the windings given in Sec.III-B and an estimated inductance ( $L_{ind}$ ) given by Eq. (25), the time constant  $K_\tau$  may be estimated by Eq. (26) [20].

$$L_{ind} = 2 \cdot N^2 \cdot L \cdot (\phi_{11} + \phi_{12}) \approx 29 \text{ mH} \quad (25)$$

$$K_\tau = \frac{L}{R} \approx \frac{29 \text{ mH}}{7\Omega} \approx 4.1 \text{ ms} \quad (26)$$

in which  $\phi_{11}$  and  $\phi_{12}$  are the proper and mutual normalized ( $L = N = I = 1$ ) magnetic fluxes, whose values are given by  $\phi_{11} = 3.3 \cdot 10^{-6} \text{ H/m}$  and  $\phi_{12} = 2.9 \cdot 10^{-7} \text{ H/m}$  [20].

Fig. 15 depicts the time response of one of the windings for a step input, showing the x-component of the magnetic field sensed by the HMR2300 magnetometer in the vertical axis of the graph. Fig. 15 shows that the magnetic field almost reach its final value between the first and the fourth points highlighted in the graph. Considering that there are five time constants in this interval of 0.129 s, the time constant is estimated as 26 ms. This practical time constant is higher than that predicted in Eq. (26), probably because the internal dynamics and electronics of the sources were not considered in the theoretical estimation. Besides this, the hypothesis that the cage model in Eq. (24) is static, *i.e.*  $B_k$  and  $I_k$  are related by a constant, still holds, since this practical time constant is almost 100 times smaller than the time constant of the PID control. Fig. 16 shows the magnetic field measured in each axis when the sources are turned on alternatively. It shows that the cage is capable of generating approximately 150  $\mu T$  in each axis and also the magnetic field variations caused by one axis in the other two when the source is turned on, which include misalignment effects in the cage/sensor and magnetic induction effects. These variations are suppressed by the PID controller.

After properly setting up the sampling time of the simulation, an orbit simulation is performed, which represents the LEO orbit of a nanosatellite. Fig. 17 shows the desired/measured magnetic fields, respectively. The percent error between the desired and the measured magnetic fields in Fig. 17 was computed for each simulation step, giving no more than 4%.

As a result, one can say that the EMF simulator is capable of providing the desired magnetic field shown in the simulation,

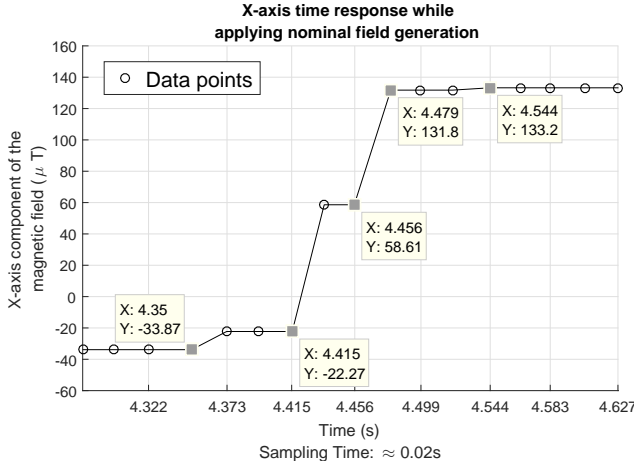


Fig. 15: Time response of a pair of coils.

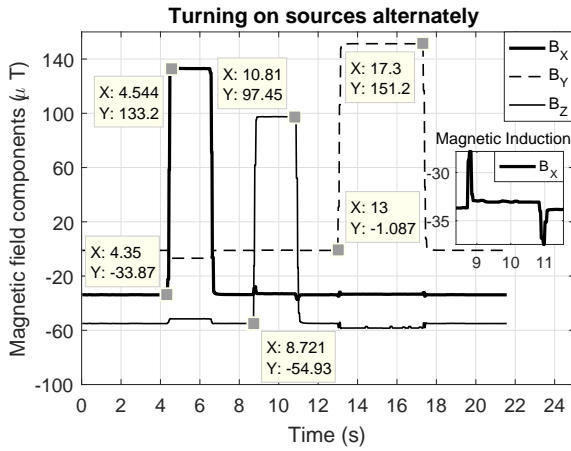


Fig. 16: Magnetic field generation capability of each axis.

which means that the tuned PID-controller works properly and the cage is capable of cancelling the laboratory environmental magnetic field and generating only the simulation field.

### B. Experiment 2: uniformity test of the magnetic field

To test the uniformity of the Helmholtz cage, the procedure described in [14] was used. In this procedure, a wooden plate graduated in centimeters is placed along the axis, aided by strings tied to the cage. Then, the HMR2300 magnetometer is placed along the plate marks with each measurement being taken every 2 cm. Considering the origin of the axis as the center of the cage, the range of measurements is  $[-100; 100]$  cm. For a specific position in the scale, 10 measurements were taken and the correspondent mean was computed. Table II shows the magnetic field and its deviations from the center value along the Y axis. The obtained magnetic field roughly shows the same theoretical uniformity calculated in Fig. 7.

Distance along axis (in cm)	-100	-80	-60	-40	-20	0 <sup>a</sup>	20	40	60	80	100
Magnetic field (in $\mu T$ )	112.57	126.33	136.14	140.13	140.69	140.39	139.93	139.59	135.57	127.81	114.15
Deviation from center (%) <sup>a</sup>	-19.81%	-10.01%	-3.02%	-0.18%	+0.22%	0%	-0.32%	-0.56%	-3.42%	-8.95%	-18.69%

<sup>a</sup>: The value at center is taken as the mean of the values in the range  $[-16; 16]$  cm to suppress noise effects in the measurements.

TABLE II: Magnetic field along cage Y-axis at nominal winding current (6.0 A).

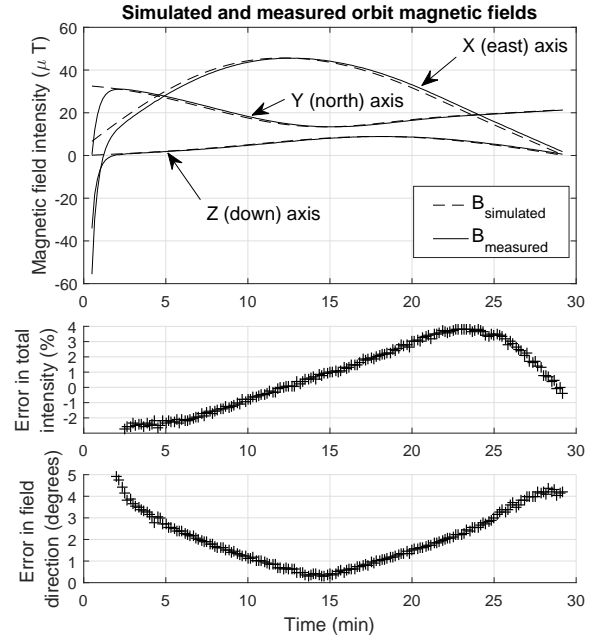


Fig. 17: Measured and simulated magnetic fields.

### C. Experiment 3: test of the magnetorquers

Testing the magnetic actuation system requires the use of both the magnetorquers and the Helmholtz cage. The Helmholtz cage is used to generate the oscillating magnetic field with which the magnetorquers will interact. In this experiment, the selected magnetic field is a  $120\mu T$  constant magnitude vector which rotates from the x-axis towards the y-axis of the cage, until it reaches a prefixed angle  $\zeta$ . When the test starts, the components of the magnetic field vector are  $B = [120 \ 0 \ 0] \mu T$  and it rotates until it becomes  $B = [120 \cos(\zeta) \ 120 \sin(\zeta) \ 0] \mu T$ , remaining in this configuration for a while before it returns to the initial value. This trajectory is repeated two times throughout the experiment.

Before starting to oscillate the field, the magnetorquers are set up at full voltage, in order to maximize the generated torque, and stay in this condition throughout the experiment. The magnetic trajectory is divided in approximately 450 samples and is executed at a sampling rate of 0.1 Hz. Fig. 18 shows the direction of the generated field calculated as

$$\angle B = \text{atan} \left( \frac{B_y}{B_x} \right) \quad (27)$$

and the yaw angle of the testbed measured with the CVADS application. The yaw angle acquired from the CVADS ranges in the  $[-180; 180]$  degrees interval, so the yaw graph was adapted to the  $[0; 360]$  degrees to preserve the continuity of the graph. Since the yaw reference adopted in Eq. (27) for the field

direction is different from the yaw reference of the testbed, the graph of Fig. 18 needs two different vertical axes, one ranging in  $[-40; 100]$  deg (field direction) and other ranging in  $[80; 220]$  deg (testbed yaw), both in 140 deg intervals. Additionally, a median filter was applied to the measurements to suppress spike errors.

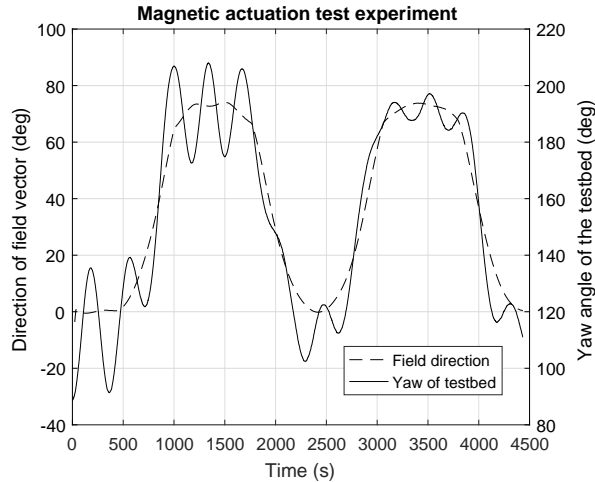


Fig. 18: Magnetic actuation in the xy plane.

Fig. 18 shows that the magnetorquers, by effect of the Helmholtz cage induced field, can provide a yaw maneuver of the testbed of approximately 90 deg in 17 minutes (first 1020 seconds). This interval and the oscillations around the reference magnetic field of the yaw angle of the testbed are consistent with the test. These oscillations are, in fact, a consequence of the low damping present on the actuation, combined with the high inertia of the testbed when compared with the torque of the magnetorquers. These two issues make it difficult for the actuators to brake the acceleration accomplished by the system. It must be also noticed that this test was performed passively, *i.e.* the magnetorquers act as simple magnets since a control action was not calculated. The aperiodic behaviour of the testbed yaw response may also be explained by the energy exchange between the testbed axes, because the testbed is not restricted to rotate about the yaw axis only, being also capable of presenting some oscillation around its roll and pitch axes throughout the experiment. These issues may be diminished with the implementation of an active control algorithm or expanding the duration of the experiment to decrease the  $\frac{dB}{dt}$  rate required by the target experiment, but this is outside of the scope of this work.

## V. CONCLUSIONS

This work has provided a detailed overview of an Earth Magnetic Field simulator for nanosatellites ADCS analyses that has been developed at the University of Brasília. The simulator is composed of an Helmholtz cage integrated with three power sources controlled by an external computer. The mathematical modeling of the simulator and the theoretical expected results have been studied before going through the description of its physical implementation details. The electri-

cal, mechanical and hardware/software aspects of the design have been detailed in the text.

HWIL tests were performed, that have validated the simulator design and ensured that it is adequate for reproducing the Earth magnetic field levels in a laboratory. The artificial magnetic field allows to host 3U CubeSats sized satellites inside the cage, maintaining satisfactory levels of uniformity. The simulator can be successfully used to activate and test magnetorquers for ADCS testing algorithms purposes, which will be object of future studies.

## ACKNOWLEDGMENT

This work was partially supported by the Federal District Research Support Foundation (FAPDF), the Coordination for the Improvement of Higher Education Personnel (CAPES) and the National Council for Scientific and Technological Development (CNPq).

## REFERENCES

- [1] M. Pastena and M. Grassi, "Optimum design of a three-axis magnetic field simulator," *IEEE Transactions on Aerospace and Electronic Systems*, vol. 38, no. 2, pp. 488–501, 2002.
- [2] M. Y. Ovchinnikov, S. Karpenko, A. Serechnitskiy, S. Tkachev, and N. Kupriyanova, "Laboratory facility for attitude control system validation and testing," in *Digest of the 6th International Symposium of IAA Small Satellites for Earth Observation*, 2007, pp. 137–140.
- [3] F. Piergentili, G. P. Candini, and M. Zannoni, "Design, manufacturing, and test of a real-time, three-axis magnetic field simulator," *IEEE Transactions on Aerospace and Electronic Systems*, vol. 47, no. 2, pp. 1369–1379, 2011.
- [4] D. Ivanov, S. Karpenko, M. Y. Ovchinnikov, D. Roldugin, and S. Tkachev, "Testing of attitude control algorithms for microsatellite "chibis-m" at laboratory facility," *Journal of Computer and Systems Sciences International*, vol. 51, no. 1, pp. 106–125, 2012.
- [5] D. S. Batista, F. Granziera, M. C. Tosin, and L. F. de Melo, "Three-axial helmholtz coil design and validation for aerospace applications," *IEEE Transactions on Aerospace and Electronic Systems*, 2017.
- [6] S. Magdaleno-Adame, J. Olivares-Galvan, E. Campero-Littlewood, R. Escarela-Perez, and E. Blanco-Brisset, "Coil systems to generate uniform magnetic field volumes," in *Excerpt from the proceedings of the COMSOL conference*, vol. 13. COSMOL, Inc, Lindsay Paterson, 2010, pp. 401–411.
- [7] R. C. d. Silva, F. C. Guimarães, J. V. L. d. Loloia, R. A. Borges, S. Battistini, and C. Cappelletti, "Tabletop testbed for attitude determination and control of nanosatellites," *Journal of Aerospace Engineering*, vol. 32, no. 1, p. 04018122, 2018.
- [8] M. Lovera and A. Astolfi, "Global magnetic attitude control of spacecraft in the presence of gravity gradient," *IEEE transactions on aerospace and electronic systems*, vol. 42, no. 3, 2006.
- [9] M. Ovchinnikov, V. Pen'ko, O. Norberg, and S. Barabash, "Attitude control system for the first swedish nanosatellite munin," *Acta Astronautica*, vol. 46, no. 2-6, pp. 319–326, 2000.
- [10] P. G. Haddox, "The development of a hardware-in-the-loop attitude determination and control simulator for illinisat-2," in *52nd Aerospace Sciences Meeting*, 2014, p. 0007.
- [11] A. Zikmund, M. Janosek, M. Ulvr, and J. Kupec, "Precise calibration method for triaxial magnetometers not requiring earths field compensation," *IEEE Transactions on Instrumentation and Measurement*, vol. 64, no. 5, pp. 1242–1247, 2015.
- [12] I. S. Kinoshita Ishioka, S. Battistini, C. Cappelletti, and R. A. Borges, "Design and development of an active magnetic actuator for attitude control system of nanosatellites," in *4th IAA Conference on Small Satellites*. International Academy of Astronautics, 2017.
- [13] G. Oliveira, P. D. Nehme, and C. Cappelletti, "Analysis and simulation of attitude determination and control for the serpens nanosatellite," in *Proceedings of 2nd IAA Conference on Dynamics and Control of Space Systems, Rome, Italy*, 2014, pp. 1–20.

- [14] J. V. Lopes de Loliola, L. Cmara van der Ploeg, R. Cardoso da Silva, F. Cardoso Guimares, R. A. Borges, G. A. Borges, S. Battistini, and C. Cappelletti, "3 axis simulator of the earth magnetic field," in *Aerospace Conference, 2018 IEEE*. IEEE, 2018.
- [15] M. Y. Ovchinnikov, D. Ivanov, N. Ivlev, S. Karpenko, D. Roldugin, and S. Tkachev, "Development, integrated investigation, laboratory and in-flight testing of chibis-m microsatellite adcs," *Acta Astronautica*, vol. 93, pp. 23–33, 2014.
- [16] S.-I. Sakai, Y. Fukushima, and H. Saito, "Design and on-orbit evaluation of magnetic attitude control system for the reimei microsatellite," in *Small Satellites for Earth Observation*. Springer, 2008, pp. 185–197.
- [17] D. Vallado, P. Crawford, R. Hujsak, and T. Kelso, "Revisiting spacetrack report# 3," in *AIAA/AAS Astrodynamics Specialist Conference and Exhibit, 2006*, p. 6753.
- [18] S. Garrido-Jurado, R. Muñoz-Salinas, F. J. Madrid-Cuevas, and M. J. Marín-Jiménez, "Automatic generation and detection of highly reliable fiducial markers under occlusion," *Pattern Recognition*, vol. 47, no. 6, pp. 2280–2292, 2014.
- [19] C. C. Foster and G. H. Elkaim, "Extension of a two-step calibration methodology to include nonorthogonal sensor axes," *IEEE Transactions on Aerospace and Electronic Systems*, vol. 44, no. 3, 2008.
- [20] J. D. Spencer and R. H. Davis, "Helmholtz coils for mil-std-462d rs101 testing," in *Electromagnetic Compatibility, 1999 IEEE International Symposium on*, vol. 2. IEEE, 1999, pp. 940–942.



Universidade de Brasília since 2013. In 2012 he was a visiting researcher at the Faculty of Aerospace Engineering, Technion - Israel Institute of Technology (Israel). In 2017 he was a visiting professor at the Departamento de Ingeniería Mecánica, Máquinas e Motores Térmicos e Fluidos, Universidad de Vigo (Spain). His main research interests are related with guidance, navigation and control of aerospace vehicles.



**Rodrigo Cardoso da Silva** received the B.S. degree in Mechatronics Engineering in 2015 and the Master's Degree in Engineering of Electronic Systems and Automation in 2018, both received from the University of Brasília, where he is currently a Ph.D. student of the Postgraduate Program of Electrical Engineering. His research interests include adaptive control, nonlinear systems, aerospace systems, optimal filtering, Lyapunov theory, embedded electronics and real-time systems.



**Igor Seiiti Kinoshita Ishioka** received the B.S. degree in Aerospace Engineering from University of Brasília in 2018. From 2014 to 2015 he participated to the SERPENS CubeSat mission working on the Assembly, Integration and Testing activities (AIT). In 2015 he was awarded with the prize of scientific initiation of University of Brasília due to the work conducted on the instrumentation of a hybrid rocket engine. From 2016 to 2017 he was an exchange student at the Institut Supérieur de l'Aéronautique et de l'Espace (ISAE-SUPAERO).



**Chantal Cappelletti** received a BSc (2005) in Aerospace Engineering, a MSc (2008) in Astronautical Engineering and a PhD (2012) in Aerospace Engineering all from Sapienza Università di Roma (Italy). She is currently an Assistant Professor at University of Nottingham (UK), where she is affiliated with the Nottingham Geospatial Institute. Previously, she was an Assistant Professor at the University of Brasilia (Brazil) and a visiting researcher at Morehead State University (USA). She is the cofounder of the Italian company GAUSS

Srl. She has led 6 satellite projects and she has been the PI of 2 missions concerning cancer cells behaviour in space. She was an Italian Space Agency delegate at the Inter-Agency Space Debris Coordination Committee. Her main research interests are related with small satellites, biomedical research in space, space debris, astrodynamics and attitude control. She is member of the International Academy of Astronautics.



**Renato Alves Borges** received a Master (2004) and Doctoral (2009) degree in Electrical Engineering from the University of Campinas and a PhD degree in Electrical Engineering from the University of New Mexico (USA) (2009). From 2009 to 2011 he held a post-doctoral fellowship from the state of Sao Paulo Research Foundation working at the School of Electrical and Computer Engineering at the University of Campinas. He is an assistant professor and currently the Head of the Electrical Engineering Department of the University of Brasília

and a control system researcher affiliated with the Laboratory of Automation and Robotics (LARA) and the Executive Coordinator of the Laboratory for Application and Innovation in Aerospace Sciences (LAICA) at the University of Brasília. His main research interests are Lyapunov stability theory, stability analysis of linear and nonlinear systems, modeling and control of rotating body, dynamic system analysis under uncertainty, and development of high altitude scientific platforms.